Analysis of *Plasmodium falciparum* myosin B ATPase activity and structure in complex with the calmodulin-like domain of its light chain MLC-B

Isa Pires[1,*], Yu-Fu Hung[1], Ulrich Bergmann[1], Justin E. Molloy[2], and Inari Kursula[1,3,*]

From the [1]Biocenter Oulu and Faculty of Biochemistry and Molecular Medicine, University of Oulu, Oulu, Finland; [2]Single Molecule Enzymology Laboratory, Francis Crick Institute, London, UK; [3]Department of Biomedicine, University of Bergen, Bergen, Norway

Edited by Enrique De La Cruz

Myosin B (MyoB) is a class 14 myosin expressed in all invasive stages of the malaria parasite, *Plasmodium falciparum*. It is not associated with the glideosome complex that drives motility and invasion of host cells. During red blood cell invasion, MyoB remains at the apical tip of the merozoite but is no longer observed once invasion is completed. MyoB is not essential for parasite survival, but when it is knocked out, merozoites are delayed in the initial stages of red blood cell invasion, giving rise to a growth defect that correlates with reduced invasion success. Therefore, further characterization is needed to understand how MyoB contributes to parasite invasion. Here, we have expressed and purified functional MyoB with the help of parasite-specific chaperones Hsp90 and Unc45, characterized its binding to actin and its known light chain MLC-B using biochemical and biophysical methods and determined its low-resolution structure in solution using small angle X-ray scattering. In addition to MLC-B, we found that four other putative regulatory light chains bind to the MyoB IQ2 motif *in vitro*. The purified recombinant MyoB adopted the overall shape of a myosin, exhibited actin-activated ATPase activity, and moved actin filaments *in vitro*. Additionally, we determined that the ADP release rate was faster than the ATP turnover number, and thus, does not appear to be rate limiting. This, together with the observed high affinity to actin and the specific localization of MyoB, may point toward a role in tethering and/or force sensing during early stages of invasion.

Malaria is an infectious disease caused by parasites of the genus *Plasmodium* that caused the death of more than 627,000 people in 2020 (1). Parasite motility, host cell invasion, and egress from the host cells is mediated by an actomyosin motor (2–4). Myosins are a diverse family of motor proteins composed of a heavy chain (100–150 kDa molecular weight) and a variable number of light chains (17–35 kDa). The heavy chain has three functional regions: A canonical N-terminal motor domain that is responsible for actin binding, ATP hydrolysis, and force generation; a light chain–binding region (lever arm) with IQ motifs where one or more calmodulin-like light chain subunits bind; and a highly variable C-terminal tail region with sites that determine the specific activities of a particular myosin. The tail region may have coiled-coil forming motifs that lead to heavy chain oligomerization and filament formation and/or globular domains that specify cargo binding, regulation of motor activity, and subcellular targeting (5–7).

Genomic analysis of the *Plasmodium* species identified six myosin heavy chain genes (5), of which myosin A (MyoA) and myosin B (MyoB) are both class 14 myosins that differ from other myosin classes in that they lack the tail region (2, 7, 8). MyoA is the best studied, as it is present in the glideosome motor complex and is the main motor responsible for generating force for motility and invasion of the red blood cell (2, 9, 10). Two light chains have been identified for MyoA: a so-called essential light chain (ELC), which occupies the first IQ motif (IQ1), and MyoA tail domain–interacting protein (MTIP), which despite its name occupies the second IQ motif (IQ2) in the neck region (9, 11–14).

MyoB, the smallest *Plasmodium* myosin, with 17 fewer residues than MyoA (7) is expressed in all invasive stages (merozoites, ookinetes, and sporozoites) (8, 15). It was first found with a fixed localization in the apical portion of merozoites (7). Later, it was shown to localize more specifically in the extreme apex of merozoites, ookinetes, and sporozoites (8, 15), overlapping with tubulin, indicative of association with the polar rings (8). This is also supported by a ring-like shape in mature ookinetes, as seen in super-resolution microscopy (15). During invasion, MyoB remains at the apical tip of merozoites and disappears once the process is completed (8). MyoB does not colocalize with MyoA, and there is no evidence of association with the glideosome protein complex (15), even though *in silico* predictions (16) and subsequent interaction studies (17) have suggested the possibility of such interactions. MyoB is not essential for parasite survival (8, 15), but it has been hypothesized to be involved in erythrocyte invasion (7). MyoB conditional KO merozoites showed reduced invasion success due to delayed initiation of parasite internalization; however, invasion into the red blood cell still proceeded, and

* For correspondence: Isa Pires, isa.paivapires@oulu.fi; Inari Kursula, inari.kursula@uib.no.

viable parasites, albeit with a small growth defect, were produced ([8], [10], [15]).

A single light chain, MLC-B, has been identified for MyoB ([8]). In ookinetes, MLC-B is positioned at the apical end early during development, 12 h before MyoB is first detected ([15]). For a myosin light chain, MLC-B is large, being composed of an EF-hand–containing calmodulin-like domain (CaMLD) at the C terminus and a large N-terminal domain of unknown function, predicted to form a coiled-coil structure ([8]). Interestingly, unlike MyoB, MLC-B is essential for parasite survival, which together with its early appearance at the apical end might suggest additional functions, independent of MyoB ([8], [15]). It is also possible that another myosin could take over some functions and interact with MLC-B in place of MyoB.

In this study, we have produced recombinant *Plasmodium falciparum* MyoB in complex with MLC-B CaMLD and performed biochemical and structural characterization of this protein complex. We show that MyoB can be expressed and purified in sufficient amount and purity for structural and biochemical studies, using a heterologous expression system, including parasite-specific chaperones for correct protein folding. The purified recombinant MyoB is an active motor with a higher affinity to actin than MyoA. The MyoB neck IQ2 region can interact, *in vitro*, with four calmodulin family light chains other than MLC-B.

Results

Parasite-specific chaperones are required for correct folding of MyoB

The expression of *P. falciparum* MyoB alone in *Spodoptera frugiperda* (*Sf*)21 insect cells resulted in very little or no soluble protein, despite extensive screening for solubilizing conditions ([Fig. 1A]). Coinfecting the cells with equal amounts of viruses for MyoB and the *P. falciparum* homolog of the chaperone Unc45 (hereafter Unc45), as described previously for MyoA ([14]), or infecting with a virus containing MyoB, Unc45, and *P. falciparum* Hsp90, did not improve the solubility of the protein ([Fig. 1A]). Soluble MyoB could be obtained by infecting the cells with two viruses, one containing MyoB-Unc45-Hsp90 and another containing Unc45, at a ratio of 10:1 (v/v) ([Fig. 1A]). The overall expression level of MyoB decreased with the addition of chaperones ([Fig. 1A]), and although the amount of soluble protein on the gels does not seem to increase substantially with the addition of surplus Unc45, this was the only condition that enabled producing useful amounts of soluble MyoB.

We and others ([8]) have been unable to purify full-length MLC-B. Likewise, copurification of this light chain with MyoB failed. Negatively stained gold particle immune electron micrographs of the *Sf*21 expression cells revealed that full-length MLC-B is severely aggregated *in cellulo* ([Fig. S1]).
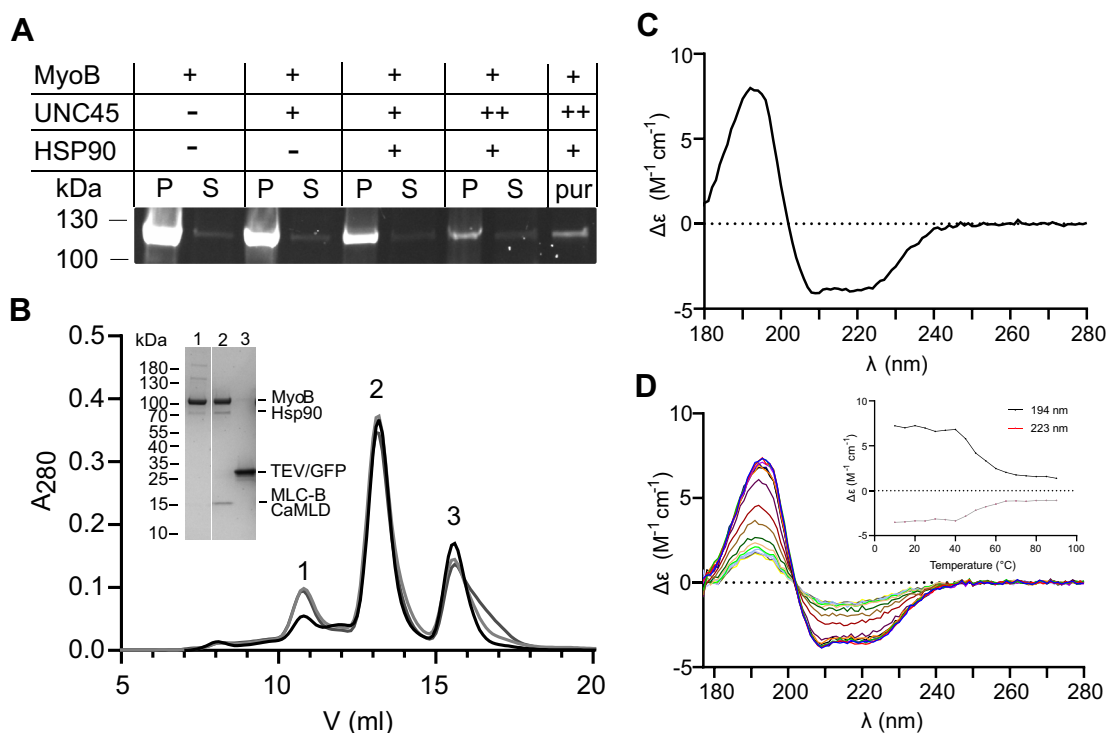

Figure 1. MyoB solubility and the MyoB–MLCB CaMLD complex purification. *A*, SDS-PAGE imaged under UV light for detection of eGFP-MyoB fusion protein. S: soluble fraction; P: insoluble fraction; pur: purified protein. Equal culture and buffer volumes were used for all samples, with the exception of pur that acts as a control. *B*, elution of MyoB–MLC-B CaMLD from a Superdex S200 10/300 column in 20 mM Tris–HCl (pH 8.5), 150 mM KCl, 0.5 mM TCEP, 5 mM MgCl$_2$, 0.1 mM EGTA at a flow rate of 0.35 ml min^{-1}. The different *black-gray* curves represent three independent purifications. The inset shows samples from the SEC peaks on SDS-PAGE. Peak 1 contains partially unfolded MyoB, peak 2 the folded MyoB–MLC-B CaMLD complex, and peak 3 Strep-tag-eGFP/TEV. *C*, SR-CD spectrum of the MyoB–MLC-B CaMLD complex. *D*, SR-CD spectra of the MyoB–MLC-B CaMLD complex at temperatures between 10 °C and 90 °C (5 °C intervals). The inset shows the change in Δε at 223 and 194 nm upon heating. CaMLD, calmodulin like-domain; MLC, myosin light chain; Myo, myosin; SEC, size-exclusion chromatography; SR-CD, synchrotron radiation-CD; TCEP, tris(2-carboxyethyl)phosphine.

Therefore, we used for all experiments a construct where the N-terminal coiled-coil region of the full-length MLC-B was removed, thus resulting in just the C-terminal CaMLD (hereafter termed MLC-B CaMLD) (8).

The stability of the neck region of myosins is often increased by the binding of light chains (18) (Fig. 2). Here, MyoB and MLC-B CaMLD were produced in different expression systems. Therefore, purified MLC-B CaMLD was added to the MyoB cell lysate immediately after cell disruption by sonication and before clarification by centrifugation. Even though the lysis buffer had a high ionic strength (500 mM NaCl), MLC-B CaMLD still bound to MyoB (Fig. 1*B*). Size-exclusion chromatography (SEC) showed that the fraction of MyoB not bound to MLC-B CaMLD eluted earlier than the MyoB–MLC-B CaMLD complex, together with Unc45 and Hsp90 (Fig. 1*B*). This suggests that this small amount of MyoB may be partially unfolded and/or aggregated (Fig. 1*B*). The MyoB–MLC-B CaMLD complex eluted as a symmetric peak (Fig. 1*B*). The molecular weight of recombinant MyoB was determined by mass spectrometry to be 93,376 Da, which corresponds very closely to the expected size 93,378.86 Da without any post-translational modifications (PTMs).

Synchrotron radiation CD spectroscopy (SR-CD) was used to evaluate the folding state and thermal stability of recombinant purified MyoB–MLC-B CaMLD. Deconvolution of SR-CD spectra indicated that the complex purified as aforementioned is composed of 36% α-helix, 14% β-sheet, 13% turn, and 37% other structure, as calculated using the BeStSel server (19). The complex is therefore folded (Fig. 1*C*), with secondary structure contents similar to other myosins (20) (Table S1). The normalized RMSD was low (0.006), indicating a strong correlation between the data and the calculated secondary structure contents. The melting temperature (T_m) of the complex was 50.6 °C, calculated from a sigmoidal fit to the peaks at 223 and 194 nm (Fig. 1*D*). The T_m of the MyoB–MLC-B CaMLD complex was slightly higher (Fig. 1*D* and Table S2) compared to the T_m values of other myosins (Table S2). This could indicate that the nucleotide-free state of MyoB is more stable than the motor domains of the previously characterized myosins. However, the stability of MyoB was measured in the presence of its light chain, contrary to the other tested myosins, which might influence the T_m value.

We then used small angle X-ray scattering (SAXS) to determine the shape and dimensions of the MyoB–MLC-B CaMLD complex in solution (Fig. S2). The shape of the scattering curve and the dimensionless Kratky plot indicate a folded, elongated protein with some flexible parts (Fig. S2, *A* and *B*). The observed maximum distance (D_{max}) of over 200 Å shows that the complex is rather extended (Fig. S2*C* and Table S3). Low-resolution *ab initio* models generated using DAMMIN (21) and GASBOR (22) show an overall shape that fits well to a monomeric myosin motor domain with a bound light chain (Fig. S2*D*). A recent high-resolution structure of the MyoA light chain complex (23) also matches the shape and dimensions of the SAXS models (Fig. S2*D*).

MyoB–MLC-B CaMLD binds actin and moves actin filaments in vitro

Consistent with our biochemical and biophysical analyses, negatively stained electron microscopy images of MyoB–MLC-B CaMLD indicated that the protein complex was homogeneous and monomeric, with no evidence of Y-shaped, two-headed, myosin dimers (Fig. 3*A*). Jasplakinolide-stabilized *P. falciparum* actin I filaments mixed, in the absence of Mg.ATP, at a ratio of 5:1 with the MyoB–MLC-B CaMLD complex appeared more rugged than jasplakinolide-stabilized actin I filaments alone and showed punctate localization of myosin-like structures on the filaments (Fig. 3*A*). However, fully decorated, arrowhead-like structures as seen for MyoA (24) were not observed. Ultracentrifugation sedimentation assays, performed in the presence or absence of Mg.ATP, showed that MyoB with or without MLC-B CaMLD cosedimented with porcine skeletal muscle α-actin (Fig. 3*B*). In the presence of ATP, there were approximately equal amounts of MyoB in the pellet and supernatant; while in the absence of ATP, most of the MyoB was in the pellet together with actin.

We conducted *in vitro* motility assays using fluorescence video microscopy to characterize the ability of MyoB to move actin filaments in the presence of Mg.ATP. MyoB was captured on a microscope coverslip either by binding nonspecifically to a surface layer of nitrocellulose or by using an anti–glutathione-*S*-transferase (GST) antibody to capture the GST-tagged MLC-B CaMLD. Both methods allow the myosin head domain to face upward. The antibody-capture method was performed in two different ways: (1) the microscope coverslip with surface-immobilized anti-GST antibody was first incubated with MLC-B CaMLD and subsequently incubated with MyoB. (2) The antibody-coated coverslip was incubated directly with the fully formed MyoB–MLC-B CaMLD complex. In the absence of Mg.ATP, immobile, rhodamine-phalloidin labeled porcine α-actin filaments were observed on the coverslip surface. Upon addition of 2 mM Mg.ATP, the actin filaments moved in a directed manner, and a small number of nonmoving filaments were also observed. The different antibody capture methods resulted in virtually no difference in actin filament gliding speed (0.23 μm s^{-1} for method 1; 0.21 μm s^{-1} for method 2). Thus, the datasets were combined for further analysis. When MyoB–MLC-B CaMLD was nonspecifically immobilized on a nitrocellulose-coated surface, the actin filament gliding speed was 0.12 ± 0.53 μm (N_{obs} = 4301), which is about 2-fold slower than the antibody-capture speed 0.22 ± 0.02 μm s^{-1} (N_{obs} = 3965) (Fig. 3*C*, Movies 1 and 2). MyoB in the absence of MLC-B CaMLD showed no filament gliding upon ATP addition (Movie 3). This was expected as the light chains are necessary for stabilization of the so-called "lever arm" region, which is required for production of force and movement (25). The speed observed for MyoB–MLC-B CaMLD was similar to that of MyoA with a single MTIP light chain (14) but about 10-fold slower compared to other studies with slightly different experimental conditions (9, 23, 26).

The rate of ADP release from the acto-MyoB–ADP complex was determined by incubating α-actin labeled with N-(1-pyrene)
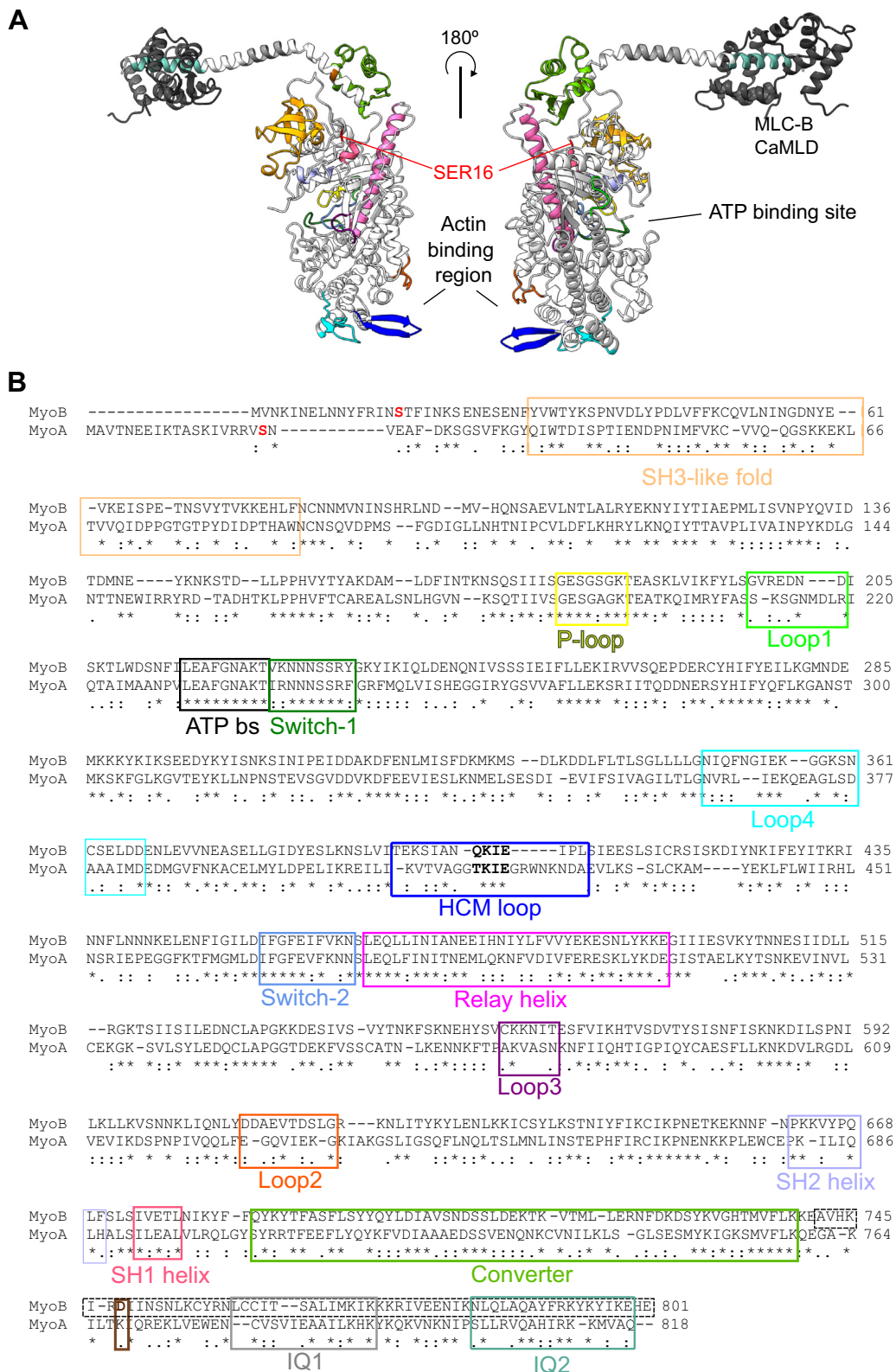
Figure 2. MyoB structure. *A*, predicted structure of MyoB generated using Alphafold (56) with functional regions of the motor domain and the lever arm highlighted. The Alphafold (56) predicted structure of MLC-B CaMLD was placed on MyoB IQ2 using superposition of the MTIP–MyoA complex (PDB code 6YCY (23)). *B*, sequence alignment of MyoA and MyoB using T-COFFEE (57) with functional regions of the motor and lever highlighted corresponding to *A* (2, 27, 53). The residues that influence the force and the speed at which the MyoA moves along actin are shown in *red* (Ser19) and *brown* (Lys769) (27). The dotted line box indicates the MyoB neck sequence (residues 742–801) used in this study. The residues in bold inside the HCM loop box (*blue*) indicate the TEDS site. IQ1 for ELC binding and IQ2 for regulatory light chain binding are shown in *gray* and *pale green*, respectively. CaMLD, calmodulin like-domain; MLC, myosin light chain; Myo, myosin; PDB, Protein Data Bank.
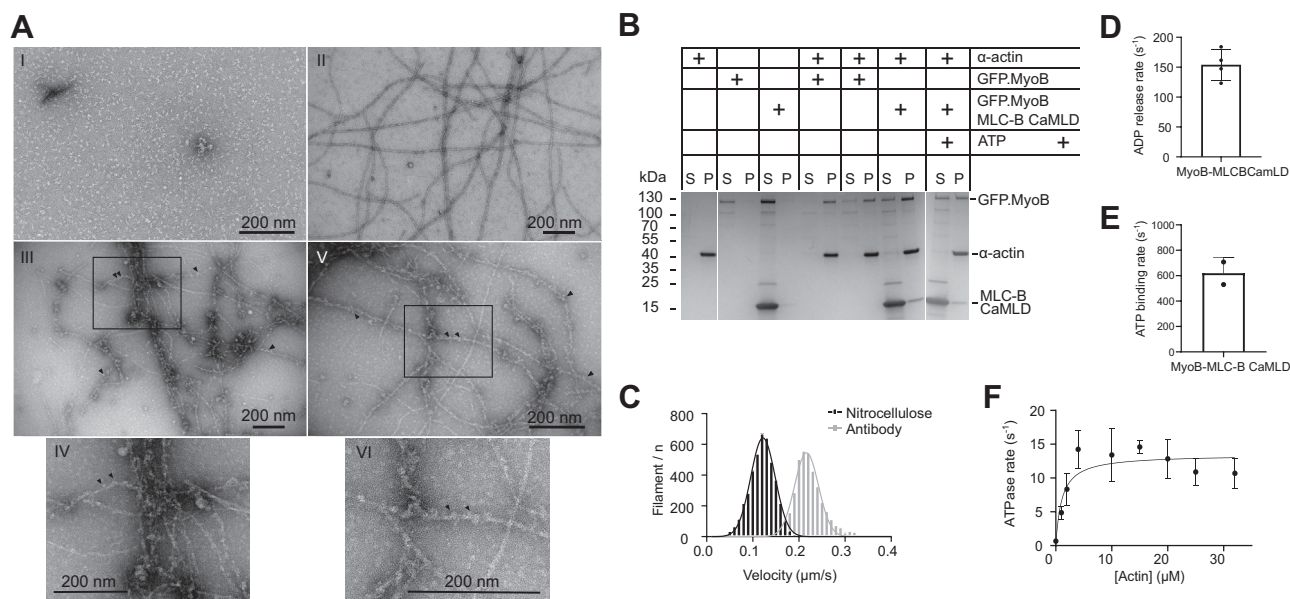
Figure 3. MyoB binding to actin. *A*, I - Negative-stained electron micrograph of MyoB–MLC-B CaMLD at 100 nM. II- Negative-stained electron micrograph of JAS-stabilized *P. falciparum* actin I at 500 nM. III and V - Negative-stained electron micrographs of MyoB–MLC-B CaMLD binding to filamentous *P. falciparum* actin I, at an actin:myosin ratio of 5:1. The scale bars represent 200 nm. *Arrowheads* indicate possible MyoB–MLC-B CaMLD particles. IV and VI – insets with magnification of represented square from II and V, respectively. *B*, cosedimentation of MyoB with filamentous α-actin, in presence or absence of ATP. *C*, motility assay of the MyoB–MLC-B CaMLD complex using nitrocellulose and antibody capture. Nitrocellulose captured data are colored *black* and the antibody captured data are colored *gray*. The antibody-capture method exhibited faster motility. *D*, the ADP release rate from the acto-[MyoB-MLC-B CaMLD].ADP complex was 154 ± 25 s^{-1}, at 24 °C (four independent experiments). *E*, rate of ATP-induced dissociation of the acto-[MyoB-MLC-B CaMLD] rigor complex was 615 s^{-1}, at 24 °C (two independent experiments). *F*, actin-activated steady-state ATPase activity of the MyoB–MLC-B CaMLD complex showed 20-fold lower K_{app} but similar k_{cat} values to the MyoA–MTIP complex (four independent experiments). All assays were performed using filamentous α-actin. CaMLD, calmodulin like-domain; MLC, myosin light chain; Myo, myosin.

iodoacetamide (NPI) with MyoB–MLC-B CaMLD and Mg.ADP and then rapidly mixing with Mg.ATP (2 mM final concentration) at 24 °C using a stopped-flow apparatus. The dissociation of MyoB from α-actin gives rise to a fluorescence increase of NPI, which reports the rate of ADP release from the motor protein, at 154 ± 25 s^{-1} (Fig. 3*D*). This is slightly slower than the previously obtained rate for MyoA at 25 °C (209 ± 39 s^{-1}) (27). Control experiments showed the NPI fluorescence change following addition of Mg.ATP (0.5 mM final) to the acto-MyoB rigor complex occurred at ~600 s^{-1} (Fig. 3*E*), confirming that the ATP-binding step did not limit our measurement of ADP release rate.

In a separate experiment, the steady-state actin-activated ATPase activity of the MyoB–MLC-B CaMLD complex was measured (Table 1). The "apparent" K_m (K_{app}) for the actin-activated ATPase activity was 1.4 μM, and the maximum actin-activated ATPase activity (k_{cat}) was 13 s^{-1} (Fig. 3*F*). The so-called coupling efficiency (k_{cat}/K_{app}) (28) was ~9 μM^{-1} s^{-1}, which is at least 2 orders of magnitude higher than reported for most myosins (Table 1) (14, 27–34). The rate of ADP release from MyoB (154 s^{-1}) was ~10-fold faster than the maximum actin-activated ATPase activity, indicating that ADP release is unlikely to be the rate-limiting step in the MyoB ATPase cycle.

MyoB interacts with MTIP and three other putative light chains

MyoA has two IQ motifs, of which IQ1 binds the essential light chain ELC and IQ2 the regulatory light chain MTIP (Fig. 2). For MyoB, MLC-B is the only light chain identified

and binds the IQ2 motif (8). *In silico* predictions and subsequent experimental data have suggested that the MyoA regulatory light chain MTIP can bind to MyoB (16, 17). However, there have been no studies on the second MyoA light chain *P. falciparum* ELC binding to MyoB. Here, pull downs of MTIP and *P. falciparum* ELC using N-terminally Strep-tagged MyoB were performed. While there was no evidence of *P. falciparum* ELC binding to the MyoB IQ motifs (Fig. 4, *A* and *B*), MTIP was pulled down using MyoB (Fig. 4, *A* and *B*), as reported previously (17). Although it was possible to pull down MTIP with MyoB *in vitro*, there is no evidence of this interaction taking place *in vivo*.

For MyoA, MTIP binding is necessary for ELC to interact with IQ1 (23, 35). Hence, pull down of *P. falciparum* ELC with the MyoB–MLC-B CaMLD complex was also attempted using the same strategy as aforementioned. However, there was still no evidence of *P. falciparum* ELC binding to the available IQ1 motif of MyoB (Fig. 4, *A* and *B*). It seems likely that *P. falciparum* ELC cannot bind to the IQ1 motif of MyoB in the presence or absence of either MTIP or MLC-B CaMLD at the IQ2 position.

The *P. falciparum* genome encodes several calmodulin-like proteins that can be putative light chains (PLCs). As an attempt to find additional light chains binding to MyoB, two approaches were used to screen whether some of the PLCs identified from the PLASMODB data base could act as binding partners for MyoB. First, for faster screening, insect cells were coinfected with viruses containing the MyoB neck (Ala742-Glu801, which contains both IQ motifs) and one PLC at a

Table 1
Steady-state kinetic parameters of MyoB–MLC-B CaMLD in comparison with selected previously characterized myosins

Myosin	k_{cat} (s^{-1})	K_{app} (µM)	k_{cat}/K_{app} (µM^{-1} s^{-1})
Pf MyoB-MLC-B CaMLD	13.0	1.4	9
Pf MyoA-MTIP-ELC (14)	11.2	37	0.3
Pf MyoA-MTIP (14)	12.9	42	0.3
Pf MyoA-MTIP-ELC (27)	138 ± 4	30.3 ± 2.3	4.6
Tg MyoA-MLC1-ELC1 (29)	84 ± 9.5	136 ± 22	0.6
Dd Myo1E (30)	2.2 ± 0.2	118 ± 20	0.017
Mm Myo5B (31)	10 ± 0.1	12.6 ± 0.4	0.8
Gg Myo5A (32)	15	1.4	11
Dd Myo2 (33)	2.6 ± 0.5	>100	<0.03
Hs Myo1C (34)	1.2 ± 0.03	1.2 ± 0.36	1
Hs Myo2b (28)	43.1	7	6
Hs β-cardiac/slow muscle I (β) (28)	5.94	39.55	0.15

The numbers in parentheses are references to previously published values.
Dd, *Dictyostelium discoideum*; Gg, *Gallus gallus*; Hs, *Homo sapiens*; Mm, *Mus musculus*; Pf, *P. falciparum*; Tg, *Toxoplasma gondii*.

time, to assess if any of the PLCs bound to either of the possibly available IQs. Three PLCs, namely PLC3 (PF3D7_0414200), PLC5 (PF3D7_0627200), and PLC7 (PF3D7_1434200) (Fig. S3), were able to bind to the MyoB neck (Fig. 4C), and their identities were confirmed by mass spectrometry. Knowing that IQ2 is occupied by MLC-B in the parasite (8), pull downs of PLC3, PLC5, and PLC7 separately, using a preformed purified complex of MyoB–MLC-B CaMLD, were performed (Fig. 4D). Only PLC5 was able to bind to the preformed MyoB–MLC-B CaMLD complex. PLC3 and PLC7 did not bind in those conditions. Thus, it is probable that their interaction with MyoB in the absence of MLC-B CaMLD occurs through IQ2.

As only PLC5 could be pulled down with the MyoB–MLC-B CaMLD complex, we attempted to purify the ternary complex by incubating the purified MyoB–MLC-B CaMLD complex with PLC5 and an excess of MLC-B CaMLD, followed by concentration and SEC. The SEC elution profile exhibited two peaks in the presence or absence of Ca^{2+}, and PLC5 was not associated with the MyoB–MLC-B CaMLD complex (Fig. S4). Thus, PLC5 being pulled down with MyoB (Fig. 4, C and D) was most probably due to PLC5 also interacting with IQ2 and competing with MLC-B CaMLD (Fig. 4, C and D). Also, the binding of either light chain is not dependent on Ca^{2+}. In conclusion, we have not been able to identify any light chain binding to the MyoB IQ1 region but several light chains can bind to its IQ2 *in vitro*.

As discussed previously, the stability of the neck region of myosins is often increased by the binding of light chains, and the presence of correct light chains can aid in expression and purification of recombinant myosins (18). The discovery of three PLCs as new binding partners for the MyoB IQ2 prompted us to try whether these PLCs might help in solubilizing MyoB for larger purification yields. A comparison of MyoB solubility after coexpression of MyoB-Unc45-Hsp90 with surplus Unc45 (10:1), PLC3 (1:1), PLC5 (1:1), or PLC7 (1:1) (v:v) was performed. Interestingly, all three PLCs were as effective in solubilizing MyoB as the method used throughout the work presented here, using a surplus of Unc45 (Fig. S5). However, none of the PLCs formed stable enough complexes to withstand the present purification protocol, as the MLC-B CaMLD does, indicating lower affinity to MyoB under these conditions than MLC-B CaMLD.
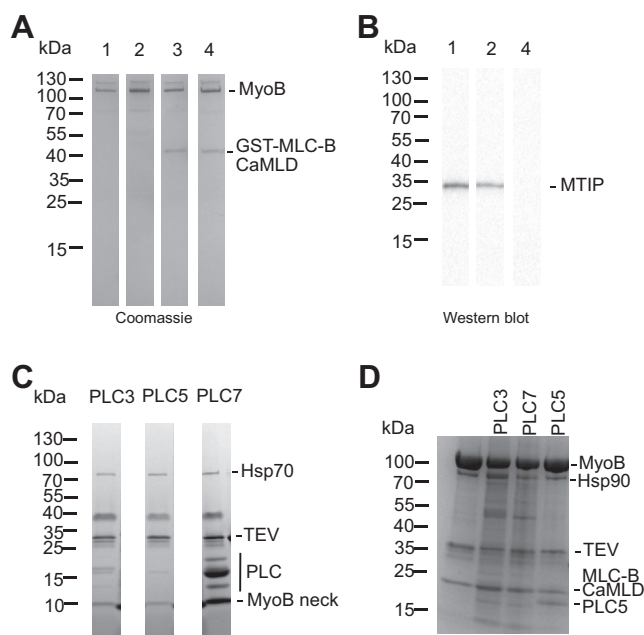
Discussion

This study aimed to shed light on the *P. falciparum* class 14 myosin, MyoB, and its interaction with several partner proteins. While much research is being conducted on MyoA, other *Plasmodium* myosins are less well studied, and their interaction partners and functions are to a large extent unknown.

Figure 4. Screening of MyoB IQ1-binding calmodulin. *A*, Coomassie brilliant blue stained SDS-PAGE gel showing the binding of MTIP, ELC, and MLC-B CaMLD to MyoB by a pull-down assay. 1: MyoB-MTIP; 2: MyoB-MTIP-ELC; 3: MyoB-GST-MLC-B CaMLD; 4: MyoB-MLC-B CaMLD-ELC. *B*, Western blot of the same samples as panel (*A*). Anti-His antibody was used to verify the presence or absence of MTIP and ELC. *C*, binding of PLCs to MyoB neck domain. PLC3, PLC5, and PLC7 were identified as light chains interacting with MyoB. *D*, pull down of PLC3, PLC7, and PLC5 using the MyoB–MLC-B CaMLD complex. The bands not labeled in the figure are contaminants from insect cell expression system. CaMLD, calmodulin like-domain; ELC, essential light chain; MLC, myosin light chain; Myo, myosin.

Chaperones and myosin light chains are essential for MyoB stability and function

Access to recombinant protein permits biophysical and biochemical analysis of myosins that may be present in only minute quantities in the native organism. Some myosins can

still only be produced in mammalian tissue culture systems (*e.g.* class 2 striated muscle myosins), while others require coexpression of specific chaperones for correct folding in baculovirus/insect cell expression systems (29, 36). The Unc45–Hsp90 chaperone complex facilitates myosin motor domain folding; Hsp90 binds Unc45 through its tetratricopeptide repeat domain and Unc45 binds myosin through its C-terminal regions. Unc45 interacts with several types of myosins, and Hsp90 binds folding intermediates shortly before their native conformation is achieved (37–39). Two interesting findings in this work were that MyoB, when compared to MyoA, required a higher ionic strength buffer for isolation (9, 14, 23, 29) and two chaperones for proper folding (Fig. 1*A*). The fact that it was necessary to infect the cells with an additional copy of the Unc45 virus to obtain soluble, correctly folded MyoB suggests that MyoB folding might require a high local concentration of Unc45. Interestingly the surplus of Unc45 was as effective in solubilizing MyoB as the presence of light chains (Fig. S5). Thus, this method could be used as a strategy to solubilize myosins, for which light chains have not been identified or that do not have predicted IQs, both of which are true for several of the so-far uncharacterized apicomplexan myosins.

As typical for myosins, also MyoB requires at least one light chain for full functionality. With a molecular weight of 78 kDa, MLC-B is an unusually large light chain, compared to other known myosin light chains, which are in the range of 17 to 35 kDa. The MLC-B N-terminal domain is prone to aggregation both *in vitro* and *in cellulo* in the recombinant expression host insect cells (Fig. S1). Given the punctate localization of MyoB *in vivo* in the parasites, this aggregation or formation of large agglomerates might be relevant for the anchoring of MyoB to the very apical tip of the parasite (8, 15).

In vivo, MyoA can be phosphorylated at Ser19, and this PTM is required for maximum motility (27). In MyoA, the interaction between phosphorylated Ser19 and Lys769 stabilizes the rigor-like state of MyoA, modulating the force and the speed at which it moves along actin (27). MyoB has a serine at position 16 (close to Ser19 of MyoA) while Lys769 in MyoA corresponds to Asp748 in the sequence alignment and the predicted structure of MyoB (Fig. 2). This substitution reverses the charge, which would have implications on the equivalent interaction in MyoB. On the other hand, residue 747 in MyoB is an arginine. Our mass spectrometry results indicate that the MyoB heavy chain has no PTMs and that the protein complex characterized here is unphosphorylated. It should be noted that Ser16 may be phosphorylated *in vivo*, but it seems that its possible effect on the myosin function may not be the same or may not follow the same mechanism as in MyoA. Further investigations on the *in vivo* phosphorylation status and high-resolution structures are required in order to gain mechanistic insight into this.

The *ab initio* SAXS model of MyoB–MLC-B CaMLD (Fig. S2) shows a model with dimensions close to those of the MyoA-MTIP-ELC crystal structure (23) if the neck with the bound light chains were in an extended conformation, not seen in the crystal structure, due to crystal packing. Additional flexibility due to the lack of a light chain bound to the IQ1 of MyoB may contribute to our failure to crystallize full-length MyoB with or without MLC-B CaMLD. The crystal structure of MyoA was obtained in complex with both light chains (23) or as a motor domain–only construct, without the neck region (27). Thus, alternative strategies need to be explored to crystallize MyoB.

MyoB–MLC-B CaMLD is an active motor

Previous studies using *P. falciparum* MyoA have shown that the maximal gliding speed depends upon the method of surface attachment, heavy chain phosphorylation state, light chain complement, and temperature (9, 14, 26, 27). Our current results with MyoB–MLC-B CaMLD were obtained using similar conditions to our previous work with MyoA (14). We found that the maximum actin gliding speed obtained using MyoB–MLC-B CaMLD was similar to that of MyoA–MTIP. It can be extrapolated that with the addition of an ELC to MyoB, the speed might double, as was seen for MyoA (9, 14, 27). However, we have not been able to identify an ELC for MyoB, and it is not clear whether one exists.

The maximum actin-activated ATPase activity determined for MyoB–MLC-B CaMLD was similar to values found for MyoA at 23 °C (14) and similar to fast skeletal muscle myosin 2 (28). MyoB showed a 20-fold lower K_{app} and at least 2 orders of magnitude higher k_{cat}/K_{app} for actin activation, indicating stronger affinity to actin. The ADP dissociation rate from MyoB on actin was approximately 10 times faster than the actin-activated steady-state ATPase rate, implying that P_i release or some other step in the actomyosin ATPase cycle is rate limiting.

High affinity to actin may be important for fixing MyoB at the apical tip and its role in internalization of the parasite during invasion (10). A contributing factor to the affinity may be sequence differences in the hypertrophic cardiomyopathy loop, in particular the TEDS site. In the TEDS site, instead of a threonine, which is an important phosphorylation site in many myosins, is a glutamine in MyoB (Fig. 2). Interestingly, this residue is a glutamine also in many other apicomplexan myosins. In fact, *P. falciparum* MyoA, which has a threonine in that position, seems to be an exception within the phylum. Of the two *P. falciparum* MyoA-actin I cryo-EM structures available, one is of the WT protein (24) and in the other one, the TEDS site threonine has been mutated to aspartic acid to mimic phosphorylation (40). In the WT structure, this side of the hypertrophic cardiomyopathy loop, including Thr417, is not directly involved in contacts with actin. In the mutant, the Oδ atom of the mutated Asp417 is within 4.7 and 4.2 Å from Lys337 and Tyr338 of actin, respectively, and could be involved in a hydrogen bond or salt bridge interaction with either of the side chains. A glutamine at this site in MyoB and many other apicomplexan myosis does not provide a negative charge (like phosphorylation or Asp/Glu) that would enable salt bridge interactions but could form hydrogen bonds to both Lys337 and Tyr338, thus contributing to the actomyosin interface.

ASBMB

J. Biol. Chem. (2022) 298(12) 102634 **7**

Taken together, our data and the cellular localization of MyoB suggest that it may serve an anchoring function during parasite invasion, helping to form and release the initial parasite–host cell contacts at the early stages of the moving junction formation. This would be analogous to the better-studied Myosin 1B, which is a low-duty ratio, force-sensitive anchor, which enables control of membrane tension and deformation (41). MyoB KO parasites take longer to invade (10), indicating that the myosin substituting for MyoB is not an effective motor for that purpose. However, the fast ADP off-rate in solution would require strong strain dependence of the rate for such a function. It is also possible that there are additional regulatory factors not yet known and absent in our study, for example, an additional slow prior ADP isomerization state, not significantly populated by ADP—or possibly the, as yet, unidentified ELC.

Several light chains bind to the MyoB IQ2 motif

In vitro, MTIP can bind to MyoB (Fig. 4*B*), as also reported before (17), but we could not detect any binding for *P. falciparum* ELC (Fig. 4, *A* and *B*). The IQ2 (Fig. 2) of MyoA has two important residues, Gln808 and Arg812, involved in MTIP binding (42), and those residues are conserved in MyoB. On the other hand, IQ1 is somewhat less conserved between MyoA and MyoB, and the alignment in the region has a gap of two residues. Thus, it is not clear whether there is an ELC that can bind to IQ1 of MyoB and whether such a light chain would be needed for maximum motility, like in MyoA.

In a simple pull-down experiment, we identified four additional light chains, which can bind to MyoB IQ2 (Fig. 4, *C* and *D*). Only further *in vivo* colocalization studies will be able to clarify the biological significance of this discovery. It can be hypothesized that the identified putative light chains may be used in the schizont or sporozoite forms, where MyoB also showed cytoplasmic distribution, besides the apical ring localization (15), or that they can be used to stabilize the myosin neck until it is bound to MLC-B. Indeed, the expression information available for these light chains indicates expression in schizonts and for PLC7 also in sporozoites (43, 44). Importantly, we have not yet been able to identify a specific light chain that binds to IQ1 of MyoB, so it remains unclear whether this IQ motif is occupied. However, we believe it is highly unlikely that this region of the MyoB heavy chain would not have an associated light chain *in vivo*.

Concluding remarks

One of the biggest obstacles to studying *Plasmodium* myosins has been in producing correctly folded, functional material using traditional methods of recombinant protein production. Here, we show that it is necessary to optimize the ratio of chaperones to myosin to produce sufficient amounts of *P. falciparum* MyoB for biochemical and biophysical analysis. This may be important for producing other myosins as well. We have determined the actin activation of MyoB ATPase activity as well as its *in vitro* gliding motility, ADP release, and ATP hydrolysis rates. Our results are directly comparable to

our previous work with MyoA and show that the affinity of MyoB to actin was markedly stronger than that of MyoA. This, together with the fact that the ADP dissociation rate from MyoB on actin is 10 times faster than the actin-activated steady-state ATPase rate, implies that P_i release or another step preceding ADP release is rate limiting and supports a tethering/force-sensing function *in vivo*. To clarify, this would require more detailed kinetic and functional characterization, including *in vivo* analyses. Finally, we found that IQ2 of MyoB was also able to bind several putative *Plasmodium* myosin light chains but *in vivo* studies are needed to find out their biological relevance.

Experimental procedures

Protein expression and purification

P. falciparum MyoB (*PF*3D7_0503600), chaperones Unc45 (*PF*3D7_1420200) and Hsp90 (*PF*3D7_0708400), and six PLCs identified from PLASMODB (PLC1 (PF3D7_0728500); PLC2 (PF3D7_0605400); PLC3 (PF3D7_0414200); PLC5 (PF3D7_0627200); PLC6 (PF3D7_1418300); PLC7 (PF3D7_1434200)), codon optimized for *Sf*21, were cloned by sequence and ligation independent cloning or the restriction enzyme method into a baculovirus transfer vector (pFL, (45)). The codon-optimized *P. falciparum Hsp90* was a kind gift from Dr Will Stanley (University of Edinburgh). Strep-tag (IBA GmbH) and eGFP were used as N-terminal tags for MyoB.

MyoB was coexpressed with Unc45 and Hsp90 to achieve correct folding, as suggested previously (29). The construct was introduced to Max Efficiency DH10Bac cells (Invitrogen), bacmids were isolated, and the gene integrations were confirmed using standard protocols (Bac-to-Bac, Invitrogen). *Sf*21 cells (Gibco) were transfected using FuGene 6 (Promega). The supernatant containing V_0 virus (virus passage zero [progeny virus]) was collected by centrifugation after 7 days of incubation at 27 °C and 325 rpm. Working virus passage 1 stocks were prepared by infecting *Sf*21 suspension cell cultures with V_0 and harvesting the supernatants after 4 to 5 days of incubation at 27 °C and 100 rpm. Protein expression was started by infecting *Sf*21 suspension cell cultures at densities between 1.0 and 2.0×10^6 cells ml^{-1}. For MyoB expression, a ratio of 10:1 (v:v) of MyoB-Unc45-Hsp90:Unc45 viruses was used. The culture was harvested at 72 h postinfection. *Sf*21 cells expressing MyoB were lysed by mild sonication using a tapped disruptor horn (Branson 450 Digital Sonifier), in 20 mM Tris–HCl pH 8.5, 500 mM NaCl, 0.5 mM tris(2-carboxyethyl)phosphine (TCEP), 10 mM $MgCl_2$, 1 mM EGTA, 1 × SigmaFast EDTA-free protease inhibitor, followed by the addition of previously purified MLC-B CaMLD. The lysate was clarified by centrifugation at 38,000*g* for 45 min and then allowed to flow through Streptactin XT matrix (IBA) twice at 4 °C. One wash with lysis buffer without protease inhibitors was followed by two consecutive washes with (i) 20 mM Tris–HCl pH 8.5, 250 mM NaCl, 0.5 mM TCEP, 5 mM $MgCl_2$, 1 mM EGTA and (ii) 20 mM Tris–HCl pH 8.5, 150 mM NaCl, 0.5 mM TCEP, 5 mM $MgCl_2$, 1 mM EGTA. The protein was eluted by on-column cleavage of the tag with

tobacco etch virus protease (TEV) and subsequently concentrated using a molecular weight concentrator (Vivaspin). The protein was filtered with a 0.22 μm pore size filter (Millipore) prior to SEC that was carried out in a Superdex S200 10/300 GL column (GE Healthcare), equilibrated with SEC buffer (20 mM Tris–HCl pH 8.5, 150 mM KCl, 0.5 mM TCEP, 5 mM MgCl$_2$, 0.1 mM EGTA). If not used immediately, the concentrated elution fractions were flash-frozen using liquid N$_2$ and stored at −70 °C.

A bacterial expression plasmid encoding the C-terminal 156 amino acids (residues 497–652) of MLC-B was kindly provided by Drs. Judith Green and Anthony Holder (Francis Crick Institute). The purification of the resulting MLC-B CaMLD (*PF*3D7_1118700) was performed as previously described (8). Purified MLC-B CaMLD was stored at −20 °C both with and without GST tag. MTIP (*PF*3D7_1246400) and *P. falciparum* ELC (*PF*3D7_1017500) were expressed and purified as described elsewhere (14). *P. falciparum* actin I was expressed and purified as previously described (46) and used freshly. *Sus scrofa* skeletal muscle α-actin was purified as described before (47, 48) and either used freshly or stored in F-form and refreshed to G-form and gel filtered prior to use.

Solubilization experiments

For solubilization tests, MyoB was expressed in *Sf*21 cells in the presence of Unc45 (1:1), Unc45-Hsp90, or Unc45-Hsp90 with surplus Unc45 (10:1) (v:v). A 50 ml culture at density 1 × 10^6 cells ml^{-1} was collected 72 h postinfection and lysed by mild sonication using a tapped disruptor horn (Branson 450 Digital Sonifier) in 20 mM Tris–HCl pH 8.5, 500 mM NaCl, 0.5 mM TCEP, 10 mM MgCl$_2$, and 1 mM EGTA, 1 × Sigma-Fast EDTA-free protease inhibitor. The soluble and insoluble fractions were separated by centrifugation at 38,000*g* for 45 min. Samples of the supernatant and pellet were then run on SDS-PAGE and imaged under UV light to detect GFP fluorescence of MyoB Strep-eGFP-tag.

The solubilization test with or without light chains was performed by coexpressing MyoB-Unc45-Hsp90 with a surplus of Unc45 virus (10:1), PLC3, PLC5, or PLC7. A 50 ml culture at density 2 × 10^6 cells ml^{-1} was collected 72 h postinfection and lysed by mild sonication using a tapped disruptor horn (Branson 450 Digital Sonifier) in 20 mM Tris–HCl pH 8.5, 500 mM NaCl, 0.5 mM TCEP, 10 mM MgCl$_2$, 1 mM EGTA, and 1 × SigmaFast EDTA-free protease inhibitor. The remaining protocol was as aforementioned (protein purification section) until the second wash. For elution, 50 mM biotin was added to wash buffer 2 (20 mM Tris–HCl pH 8.5, 150 mM NaCl, 0.5 mM TCEP, 5 mM MgCl$_2$, and 1 mM EGTA). Samples were run on SDS-PAGE and stained with Coomassie brilliant blue.

Mass spectrometry

Protein masses were determined using LC-MS with an Aquity UPLC system (Waters) linked to a Q-ExactivePlus mass spectrometer. A BioResolve RP mAB Polyphenyl column 2.1 × 50 mm was developed with a gradient comprising 0.1%

formic acid (A) and 0.5% formic acid in acetonitrile (B) with a flow rate of 0.4 ml/min and initial conditions 5% B; 0.5 min: 10% B; 9 min: 60% B; 10 min 80% B; 11 min 5% B. The mass spectrometer was operated in positive mode with resolution 17,500 and m/z range 400 to 4000. Automatic gain control and maximum injection time were set to 3 × 10^6 and 200 msec, respectively. Raw data were processed with BioPharmaFinder (Thermo) using the Respect option with standard settings suitable for proteins of MyoB molecular weight.

Synchrotron radiation CD spectroscopy

The secondary structure contents and folding state of the MyoB–MLC-B CaMLD complex were assessed using SR-CD. Protein concentrations between (measured using A_{280}) 1.0 to 1.7 mg ml^{-1}, previously dialyzed into a far-UV compatible buffer (10 mM Tris–HCl pH 8.5, 150 mM KF, 5 mM MgSO$_4$, 0.5 mM TCEP) were used. CD spectra were recorded between 170 to 280 nm at the AU-CD beamline on ASTRID2 at ISA at 10 °C in 100-μm pathlength closed circular cells. Thermal stability spectra were obtained from 10 °C to 90 °C, using a 5 °C increment. Data were deconvoluted using the BeStSel server (19), using smoothed data between 175 to 250 nm. T_m data were calculated from a sigmoidal fit to the peaks at 223 and 194 nm using GraphPad Prism 9 (GraphPad Software Inc).

SAXS

SAXS was used to analyze low-resolution structural features of MyoB–MLC-B CaMLD. SAXS data were collected at the P12 BioSAXS beamline at the PETRA III storage ring (EMBL/DESY). A concentrated sample of MyoB–MLC-B CaMLD at 3 mg ml^{-1} was dialyzed against the buffer, 20 mM Tris–HCl pH 8.5, 150 mM KCl, 5 mM MgCl$_2$, 0.1 mM EGTA, 0.5 mM TCEP, for 6 h at 4 °C. A dilution series and their corresponding buffers were measured at room temperature (RT). The automatically processed data were further analyzed using ScÅtter (49) and the ATSAS package (50). *Ab initio* models were generated using DAMMIN (21) and GASBOR (22). ChimeraX 1.1 was used for preparing the figures (51).

Actin cosedimentation assays

To assess the binding of MyoB and MyoB–MLC-B CaMLD to α-actin (prepared as described before (52)), a cosedimentation assay was performed. GFP.MyoB was purified without the addition of light chain (20 mM Tris pH 8.5, 150 mM NaCl, 5 mM MgCl2, 1 mM EGTA, 0.5 mM TCEP) and was not submitted to a SEC polishing step. The light chain MLC-B CaMLD was added to half of purified GFP.MyoB. GFP.MyoB was concentrated (Vivaspin) up to 2 μM, and GFP.MyoB MLC-B CaMLD was concentrated to 15 μM. α-actin in G-buffer (10 mM Tris–HCl pH 7.5, 0.2 mM CaCl$_2$, 0.5 mM ATP, and 0.5 mM TCEP) was dialyzed against KMg50 buffer (10 mM imidazole, pH 7.0, 50 mM KCl, 1 mM MgCl$_2$, 1 mM EGTA, 1 mM DTT) overnight (52). The polymerized α-actin (stock concentration 33 μM) was then mixed to 4 μM with 1 mM GFP.MyoB or 4 mM GFP.MyoB–MLC-B CaMLD in the absence or presence of 1 mM Mg.ATP (final

concentrations). Filaments were sedimented at 435,000g for 1 h at RT. Both pellet and supernatant fractions were examined using SDS-PAGE with Coomassie brilliant blue staining.

In vitro *motility assays*

In vitro motility assays were performed as previously described (14), with the following exceptions: the nitrocellulose-coated coverslips were incubated with protein or with anti-GST antibody (Invitrogen) for 4 min. The anti-GST antibody captures the GST tag of MLC-B CaMLD. The MyoB–MLC-B CaMLD complex was used at concentrations of 0.84 mg ml^{-1} for nitrocellulose capture or 0.84 and 0.42 mg ml^{-1} for anti-GST tag capture.

Actin-activated ATPase assay

The actin-activated ATPase activity of MyoB–MLC-B CaMLD was estimated using a NADH reduced–coupled assay to quantify the rate of ATP hydrolysis, as described before (52). The assay buffer contained 100 units ml^{-1} lactate dehydrogenase, 500 units ml^{-1} pyruvate kinase, 2.5 mM phospho(enol)pyruvate, 2 mM ATP, and 0.3 mM NADH in KMg50 buffer (50 mM KCl, 2 mM MgCl$_2$, 1 mM EGTA, 2 mM DTT, 10 mM imidazole, pH 7.0). The MyoB–MLC-B CaMLD complex was added to a final concentration of 0.15 μM, and jasplakinolide-stabilized filamentous α-actin (52) was added at concentrations ranging between 0 to 25 μM. The rate of ATP hydrolysis was calculated from the rate of change in NADH absorbance, measured in a Tecan SPARK spectrophotometer at 340 nm. The experiments were conducted at 23 °C. The data were fit to the Michaelis–Menten equation, using nonlinear regression with a least-squares fit in GraphPad Prism 9.

Transient kinetics

Transient kinetics experiments were performed in a stopped-flow spectrophotometer (Hi-Tech Scientific) to assess the ADP release rate of MyoB and the ATP induced actomyosin dissociation. A monochromator with a 2 nm bandpass was used for fluorescence excitation, and a 400 nm cutoff filter was used to measure fluorescence emission. NPI α-actin, labeled and prepared as described before (46), was excited at 365 nm. All experiments were performed in KMg50 buffer (50 mM KCl, 2 mM MgCl$_2$, 1 mM EGTA, 2 mM DTT, 10 mM imidazole, pH 7.0) at 24 °C. For the ADP release assay, the concentrations after mixing in the stopped-flow cell were 1 μM MyoB–MLC-B CaMLD, 1 μM α-actin, 250 μM ADP, and 2 mM ATP. The ADP release rates were obtained with the software provided with the instrument (Kinetic Studio 5), where 10 to 15 traces per protein preparation (four independent protein preparations) were averaged before fitting to an exponential. Nonlinear least squares fitting of the data was conducted in Graphpad Prism 9.0. For the ATP-induced actomyosin dissociation assay, the concentrations after mixing in the stopped-flow cell were 0.5 μM MyoB–MLC-B CaMLD, 0.5 μM α-actin. The ATP-induced dissociation rates were obtained with the software provided with the instrument (Kinetic Studio 5), where 11 to 15 traces per protein preparation (two independent protein preparations) were averaged before fitting to a one-exponential. The observed rates *versus* ATP concentration were fitted by a hyperbola using Graphpad Prism 9.0.

Negative stain electron microscopy

The interactions of MyoB with filamentous α-actin and *P. falciparum* actin I were analyzed by diluting both proteins into 20 mM Tris–HCl pH 8.5, 5 mM MgCl$_2$, 0.1 mM EGTA, 150 mM KCl, and 0.5 mM TCEP. Filamentous actin (final concentration of 500 nM) was mixed with myosin (final concentration of 100 nM), and 5 μl of the sample were applied and incubated for 45 s on a glow-discharged formvar-coated copper grid (standard hexagonal grid with mesh size 300) with a layer of evaporated carbon. The formvar coating and carbon evaporation were carried out in-house. After incubation, the excess liquid was blotted with filter paper and the grid stained twice with 1% (w/v) uranyl acetate (5 and 60 s, respectively), the excess liquid was blotted using filter paper, and the grid was left to dry in air. The grids were imaged using a Tecnai G2 Spirit microscope at 120 kV.

Pulldown assays

For pulldown assays, MyoB, MLC-B CaMLD, and the known MyoA light chains, MTIP and ELC, were expressed separately and purified individually as described previously (Protein expression and purification section), without removing the tags. The tags were left intact by not using TEV/3C and the proteins were immediately submitted to SEC polishing after the affinity purification. The proteins were incubated with each other in different combinations at a concentration of 20 μM for 30 min at RT, as follows: MyoB-MTIP-ELC; MyoB-MTIP, MyoB-MLC-B CaMLD, and MyoB-MLC-B CaMLD-ELC. MyoB and any interacting light chains were bound to Streptactin XT resin *via* the MyoB Strep-tag in 20 mM Tris–HCl pH 8.5, 150 mM KCl, 5 mM MgCl$_2$, 0.1 mM EGTA, and 0.5 mM TCEP. The resin was washed with 50 column volumes of the same buffer. Elution was performed by the addition of 50 mM biotin to the same buffer. Samples were taken of all steps and prepared for SDS-PAGE and Western blotting analysis.

For the putative light chain initial screening, the MyoB neck domain (Ala742-Glu801) was coexpressed with the different PLCs in *Sf*21 cells. The PLCs contained a His-tag with a human rhinovirus 3C protease cutting site, and MyoB neck domain contained a Strep-tag with a TEV cutting site. The cell pellets were resuspended in lysis buffer (20 mM Tris–HCl pH 7.5, 250 mM NaCl, 0.5 mM TCEP, 5 mM imidazole, 1 mM CaCl$_2$, 1 × SigmaFast EDTA-free protease inhibitor) and lysed by sonication (Branson 450 Digital Sonifier). The lysate was clarified by centrifugation (38,000g, 45 min). The soluble fraction was incubated for 1 h at 4 °C, under gentle agitation, with HisPur nitrilotriacetate nickel agarose resin (Thermo) equilibrated with lysis buffer. One wash with lysis buffer without protease inhibitors was followed by two consecutive

washes with (i) 20 mM Tris–HCl pH 7.5, 500 mM NaCl, 0.5 mM TCEP, 10 mM imidazole, 1 mM CaCl$_2$ and (ii) 20 mM Tris–HCl pH 7.5, 150 mM NaCl, 0.5 mM TCEP, 15 mM imidazole, 1 mM CaCl$_2$. The protein complexes were eluted by on-column cleavage of MyoB neck domain using TEV and subsequently concentrated using a centrifugal concentrator (Millipore). The samples were analyzed using SDS-PAGE, and gel bands representing PLCs were excised from the gel and analyzed using mass spectrometry. After the identification of the interacting PLC, full-length MyoB with or without MLC-B CaMLD bound was purified as described earlier until the wash step 2, then the purified PLC was allowed to incubate with the resin-containing MyoB for at least 30 min, followed by two consecutive washes with (i) 20 mM Tris–HCl pH 7.5, 500 mM NaCl, 0.5 mM TCEP, 10 mM imidazole, 1 mM CaCl$_2$ and (ii) 20 mM Tris–HCl pH 7.5, 150 mM NaCl, 0.5 mM TCEP, 15 mM imidazole, 1 mM CaCl$_2$. On-column cleavage was used as an elution strategy using 20 mM Tris–HCl pH 7.5, 150 mM NaCl, 0.5 mM TCEP, 15 mM imidazole, 1 mM CaCl$_2$, supplemented with TEV.

Data availability

All the relevant data and plasmids used to support the findings of this study are available upon request from the corresponding authors.

Conflict of interest—The authors declare that they have no conflicts of interest with the contents of this article.

Abbreviations—The abbreviations used are: CaMLD, calmodulin like-domain; ELC, essential light chain; MLC-B, myosin light chain B; Myo, myosin; NPI, N-(1-pyrene)iodoacetamide; PLC, putative light chain; PTM, posttranslational modifications; SAXS, small-angle X-ray scattering; SEC, size-exclusion chromatography; SR-CD, synchrotron radiation CD spectroscopy; TCEP, tris(2-carboxyethyl)phosphine.

References

1. *World Malaria Report 2021. Geneva: World Health Organization.* (2021). Licence: CC BY-NC-SA 3.0 IGO
2. Farrow, R. E., Green, J., Katsimitsoulia, Z., Taylor, W. R., Holder, A. A., and Molloy, J. E. (2011) The mechanism of erythrocyte invasion by the malarial parasite, Plasmodium falciparum. *Semin. Cell Dev. Biol.* **22**, 953–960
3. Boucher, L. E., and Bosch, J. (2015) The apicomplexan glideosome and adhesins - structures and function. *J. Struct. Biol.* **190**, 93–114
4. Frénal, K., Dubremetz, J. F., Lebrun, M., and Soldati-Favre, D. (2017) Gliding motility powers invasion and egress in Apicomplexa. *Nat. Rev. Microbiol.* **15**, 645–660
5. Foth, B. J., Goedecke, M. C., and Soldati, D. (2006) New insights into myosin evolution and classification. *Proc. Natl. Acad. Sci. U. S. A.* **103**, 3681–3686
6. Hartman, M. A., Finan, D., Sivaramakrishnan, S., and Spudich, J. A. (2011) Principles of unconventional myosin function and targeting. *Annu. Rev. Cell Dev. Biol.* **27**, 133–155
7. Chaparro-Olaya, J., Dluzewski, A. R., Margos, G., Wasserman, M. M., Mitchell, G. H., Bannister, L. H., *et al.* (2003) The multiple myosins of malaria: the smallest malaria myosin, Plasmodium falciparum myosin-B (Pfmyo-B) is expressed in mature schizonts and merozoites. *Eur. J. Protistol.* **39**, 423–427
8. Yusuf, N. A., Green, J. L., Wall, R. J., Knuepfer, E., Moon, R. W., Schulte-Huxel, C., *et al.* (2015) The Plasmodium class XIV Myosin, MyoB, has a distinct subcellular location in invasive and motile stages of the malaria parasite and an unusual light chain. *J. Biol. Chem.* **290**, 12147–12164
9. Bookwalter, C. S., Tay, C. L., McCrorie, R., Previs, M. J., Lu, H., Krementsova, E. B., *et al.* (2017) Reconstitution of the core of the malaria parasite glideosome with recombinant Plasmodium class XIV myosin A and Plasmodium actin. *J. Biol. Chem.* **292**, 19290–19303
10. Blake, T. C. A., Haase, S., and Baum, J. (2020) Actomyosin forces and the energetics of red blood cell invasion by the malaria parasite Plasmodium falciparum. *PLoS Pathog.* **16**, 1–25
11. Baum, J., Richard, D., Healer, J., Rug, M., Krnajski, Z., Gilberger, T. W., *et al.* (2006) A conserved molecular motor drives cell invasion and gliding motility across malaria life cycle stages and other apicomplexan parasites. *J. Biol. Chem.* **281**, 5197–5208
12. Bergman, L. W., Kaiser, K., Fujioka, H., Coppens, I., Daly, T. M., Fox, S., *et al.* (2003) Myosin A tail domain interacting protein (MTIP) localizes to the inner membrane complex of Plasmodium sporozoites. *J. Cell Sci.* **116**, 39–49
13. Bosch, J., Turley, S., Roach, C. M., Daly, T. M., Bergman, L. W., and Hol, W. G. J. (2007) The closed MTIP-myosin A-tail complex from the malaria parasite invasion machinery. *J. Mol. Biol.* **372**, 77–88
14. Green, J. L., Wall, R. J., Vahokoski, J., Yusuf, N. A., Ridzuan, M. A., Stanway, R. R., *et al.* (2017) Compositional and expression analyses of the glideosome during the Plasmodium life cycle reveal an additional myosin light chain required for maximum motility. *J. Biol. Chem.* **292**, 17857–17875
15. Wall, R. J., Zeeshan, M., Katris, N. J., Limenitakis, R., Rea, E., Stock, J., *et al.* (2019) Systematic analysis of Plasmodium myosins reveals differential expression, localisation, and function in invasive and proliferative parasite stages. *Cell. Microbiol.* **21**, e13082
16. Hernández, P. C., Morales, L., Castellanos, I. C., Wasserman, M., and Chaparro-Olaya, J. (2017) Myosin B of Plasmodium falciparum (PfMyoB): in silico prediction of its three-dimensional structure and its possible interaction with MTIP. *Parasitol. Res.* **116**, 1373–1382

17. Hernández, P. C., Wasserman, M., and Chaparro-Olaya, J. (2018) *In vitro* interaction between Plasmodium falciparum myosin B (PfMyoB) and myosin A tail interacting protein (MTIP). *Parasitol. Res.* **117**, 3437–3446

18. Hartman, M. A., and Spudich, J. A. (2012) The myosin superfamily at a glance. *J. Cell Sci.* **125**, 1627–1632

19. Micsonai, A., Wien, F., Kernya, L., Lee, Y. H., Goto, Y., Réfrégiers, M., *et al.* (2015) Accurate secondary structure prediction and fold recognition for circular dichroism spectroscopy. *Proc. Natl. Acad. Sci. U. S. A.* **112**, E3095–E3103

20. Coureux, P. D., Sweeney, H. L., and Houdusse, A. (2004) Three myosin V structures delineate essential features of chemo-mechanical transduction. *EMBO J.* **23**, 4527–4537

21. Svergun, D. I. (1999) Restoring low resolution structure of biological macromolecules from solution scattering using simulated annealing. *Biophys. J.* **76**, 2879–2886

22. Svergun, D. I., Petoukhov, M. V., and Koch, M. H. J. (2001) Determination of domain structure of proteins from x-ray solution scattering. *Biophys. J.* **80**, 2946–2953

23. Moussaoui, D., Robblee, J. P., Auguin, D., Krementsova, E. B., Haase, S., Blake, T. C. A., *et al.* (2020) Full-length Plasmodium falciparum myosin a and essential light chain pfelc structures provide new anti-malarial targets. *Elife* **9**, e60581

24. Vahokoski, J., Calder, L. J., Lopez, A. J., Molloy, J. E., Rosenthal, I., and Kursula, I. (2022) High-resolution structures of malaria parasite acto-myosin and actin filaments. *PLoS Pathog.* **18**, e1010408

25. Block, S. M. (1996) Fifty ways to love your lever: myosin motors. *Cell* **87**, 151–157

26. Green, J. L., Martin, S. R., Fielden, J., Ksagoni, A., Grainger, M., Yim Lim, B. Y. S., *et al.* (2006) The MTIP-myosin A complex in blood stage malaria parasites. *J. Mol. Biol.* **355**, 933–941

27. Robert-Paganin, J., Robblee, J. P., Auguin, D., Blake, T. C. A., Bookwalter, C. S., Krementsova, E. B., *et al.* (2019) Plasmodium myosin A drives parasite invasion by an atypical force generating mechanism. *Nat. Commun.* **10**, 3286

28. Johnson, C. A., Walklate, J., Svicevic, M., Mijailovich, S. M., Vera, C., Karabina, A., *et al.* (2019) The ATPase cycle of human muscle myosin II isoforms: adaptation of a single mechanochemical cycle for different physiological roles. *J. Biol. Chem.* **294**, 14267–14278

29. Bookwalter, C. S., Kelsen, A., Leung, J. M., Ward, G. E., and Trybus, K. M. (2014) A toxoplasma gondii class XIV myosin, expressed in Sf9 cells with a parasite co-chaperone, requires two light chains for fast motility. *J. Biol. Chem.* **289**, 30832–30841

30. Dürrwang, U., Fujita-Becker, S., Erent, M., Kull, F. J., Tsiavaliaris, G., Geeves, M. A., *et al.* (2006) Dictyostelium myosin-IE is a fast molecular motor involved in phagocytosis. *J. Cell Sci.* **119**, 550–558

31. Heissler, S. M., Chinthalapudi, K., and Sellers, J. R. (2017) Kinetic signatures of myosin-5B, the motor involved in microvillus inclusion disease. *J. Biol. Chem.* **292**, 18372–18385

32. De La Cruz, E. M., Wells, A. L., Rosenfeld, S. S., Ostap, E. M., and Sweeney, H. L. (1999) The kinetic mechanism of myosin V. *Proc. Natl. Acad. Sci. U. S. A.* **96**, 13726–13731

33. Venugopal, K., Hentzschel, F., Valkiūnas, G., and Marti, M. (2020) Plasmodium asexual growth and sexual development in the haematopoietic niche of the host. *Nat. Rev. Microbiol.* **18**, 177–189

34. Mezgueldi, M. El, Tang, N., Rosenfeld, S. S., and Ostap, E. M. (2002) The kinetic mechanism of myo1e (human myosin-IC). *J. Biol. Chem.* **277**, 21514–21521

35. Pazicky, S., Dhamotharan, K., Kaszuba, K., Mertens, H. D. T., Gilberger, T., Svergun, D., *et al.* (2020) Structural role of essential light chains in the apicomplexan glideosome. *Commun. Biol.* **3**, 568

36. Bird, J. E., Takagi, Y., Billington, N., Strub, M. P., Sellers, J. R., and Friedman, T. B. (2014) Chaperone-enhanced purification of unconventional myosin 15, a molecular motor specialized for stereocilia protein trafficking. *Proc. Natl. Acad. Sci. U. S. A.* **111**, 12390–12395

37. Barral, J. M., Hutagalung, A. H., Brinker, A., Hartl, F. U., and Epstein, H. F. (2002) Role of the myosin assembly protein UNC-45 as a molecular chaperone for myosin. *Science* **295**, 669–671

38. Kim, J., Löwe, T., and Hoppe, T. (2008) Protein quality control gets muscle into shape. *Trends Cell Biol.* **18**, 264–272

39. Liu, L., Srikakulam, R., and Winkelmann, D. A. (2008) Unc45 activates Hsp90-dependent folding of the myosin motor domain. *J. Biol. Chem.* **283**, 13185–13193

40. Robert-Paganin, J., Xu, X. P., Swift, M. F., Auguin, D., Robblee, J. P., Lu, H., *et al.* (2021) The actomyosin interface contains an evolutionary conserved core and an ancillary interface involved in specificity. *Nat. Commun.* **12**, 1892

41. Heissler, S. M., and Sellers, J. R. (2014) Myosin light chains: teaching old dogs new tricks. *Bioarchitecture* **4**, 169–188

42. Jones, M. L., Collins, M. O., Goulding, D., Choudhary, J. S., and Rayner, J. C. (2012) Analysis of protein palmitoylation reveals a pervasive role in Plasmodium development and pathogenesis. *Cell Host & Microbe* **12**, 246–258

43. Rovira-Graells, N., Gupta, A. P., Planet, E., Crowley, V. M., Mok, S., Ribas de Pouplana, L., *et al.* (2012) Transcriptional variation in the malaria parasite Plasmodium falciparum. *Genome Res.* **22**, 925–938

44. Gómez-Díaz, E., Yerbanga, R. S., Lefèvre, T., Cohuet, A., Rowley, M. J., Bosco Ouedraogo, J., *et al.* (2016) Epigenetic regulation of Plasmodium falciparum clonally variant gene expression during development in Anopheles gambiae. *Sci. Rep.* **7**, 40655

45. Fitzgerald, D. J., Berger, P., Schaffitzel, C., Yamada, K., Richmond, T. J., and Berger, I. (2006) Protein complex expression by using multigene baculoviral vectors. *Nat. Methods* **3**, 1021–1032

46. Kumpula, E. P., Pires, I., Lasiwa, D., Piirainen, H., Bergmann, U., Vahokoski, J., *et al.* (2017) Apicomplexan actin polymerization depends on nucleation. *Sci. Rep.* **7**, 12137

47. Pardee, J. D., and Spudich, J. A. (1982) Purification of muscle actin. *Meth. Enzymol.* **85**, 164–181

48. Ignatev, A., Bhargav, S. P., Vahokoski, J., Kursula, P., and Kursula, I. (2012) The Lasso segment is required for functional dimerization of the Plasmodium Formin 1 FH2 domain. *PLoS One* **7**, e33586

49. Förster, S., Apostol, L., and Bras, W. (2010) Scatter: software for the analysis of nano- and mesoscale small-angle scattering. *J. Appl. Crystallogr.* **43**, 639–646

50. Franke, D., Petoukhov, M. V., Konarev, P. V., Panjkovich, A., Tuukkanen, A., Mertens, H. D. T., *et al.* (2017) Atsas 2.8: a comprehensive data analysis suite for small-angle scattering from macromolecular solutions. *J. Appl. Crystallogr.* **50**, 1212–1225

51. Pettersen, E. F., Goddard, T. D., Huang, C. C., Meng, E. C., Couch, G. S., Croll, T. I., *et al.* (2021) UCSF ChimeraX: structure visualization for researchers, educators, and developers. *Protein Sci.* **30**, 70–82

52. De La Cruz, E. M., and Michael Ostap, E. (2009) Chapter 6 kinetic and equilibrium analysis of the myosin ATPase. *Meth. Enzymol.* **455**, 157–192

53. Colegrave, M., and Peckham, M. (2014) Structural implications of β-cardiac myosin heavy chain mutations in human disease. *Anat. Rec.* **297**, 1670–1680

54. Ponomarev, M. A., Furch, M., Levitsky, D. I., and Manstein, D. J. (2000) Charge changes in loop 2 affect the thermal unfolding of the myosin motor domain bound to F-actin. *Biochemistry* **39**, 4527–4532

55. Radke, M. B., Taft, M. H., Stapel, B., Hilfiker-Kleiner, D., Preller, M., and Manstein, D. J. (2014) Small molecule-mediated refolding and activation of myosin motor function. *Elife* **3**, e01603

56. Jumper, J., Evans, R., Pritzel, A., Green, T., Figurnov, M., Ronneberger, O., *et al.* (2021) Highly accurate protein structure prediction with AlphaFold. *Nature* **596**, 583–589

57. Di Tommaso, P., Moretti, S., Xenarios, I., Orobitg, M., Montanyola, A., Chang, J. M., *et al.* (2011) T-coffee: a web server for the multiple sequence alignment of protein and RNA sequences using structural information and homology extension. *Nucleic Acids Res.* **39**, W13–W17

ASBMB